PHYSICAL REVIEW FLUIDS **3**, 063902 (2018)

Stability of melt flow during magnetic sonication in a floating zone configuration

I. Grants[1,2] and G. Gerbeth[2]

[1] *University of Latvia, Institute of Physics, Miera iela 32, LV-2169 Salaspils, Latvia*

[2] *Helmholtz-Zentrum Dresden-Rossendorf, Bautzner Landstr. 400, 01328 Dresden, Germany*

(Received 19 December 2017; published 19 June 2018)

This paper considers the linear stability of a liquid metal flow driven by superimposed alternating and static axial magnetic fields in the floating zone configuration. A simple model is constructed that assumes a slight axial variation of the flow-driving radial magnetic force and a low-to-moderate skin effect. This force drives two symmetrical flow tori. Formation of the field-parallel layer is observed for a strong static field. In this regime the instability sets in as a standing azimuthal wave around the circumference of the cylindrical melt volume near its midplane. The length of this wave scales with the thickness of the parallel layer. The instability criterion may be formulated in terms of an interaction parameter reaching its critical value at around 525.

DOI: 10.1103/PhysRevFluids.3.063902

I. INTRODUCTION

A contactless excitation of power ultrasound in molten metals is possible by a static magnetic field applied together with induction heating [1,2]. This might be a useful tool to disperse ceramic particles in metal matrix composites or particle-loaded master alloys. Recently this principle has been demonstrated for the dispersion of SiC nanoparticles in an aluminum alloy matrix [3]. The contactless technique is most advantageous for higher temperature alloys, when a mechanical excitation of ultrasound [4,5] may become complicated by erosion of the sonotrode in a highly aggressive melt. For the contactless magnetic approach the acoustic pressure is proportional to the product of alternating and static components of the magnetic field, with the former being much lower than the latter [2]. It is, therefore, meaningful to increase the alternating component as much as possible. That, however, is limited by an excessive induction heating. Efficient cooling of the molten zone is one way to counteract the threat of overheating. The floating zone configuration offers such a possibility. Another option is to keep the induction frequency low. These two options are central for the model developed in this study. The problem considered here is basically concerned with the flow that arises as a side product during the magnetic sonication. Ideally, the alternating magnetic field induces a purely irrotational magnetic force distribution [2]. However, there is some practically unavoidable rotational part due to the finite height of the induction coil as well as the difference in electrical conductivities in solid and liquid phases. This rotational part drives a melt flow that may be beneficial for the ultimate goal of uniform particle dispersion. The static magnetic field, in turn, counters this flow. The same acoustic pressure being proportional to the product of static and alternating magnetic field components may be achieved by various ratios between them. Thus, there is some freedom to design the process with certain flow properties (stronger or weaker, stable or turbulent). Knowledge of the flow and its stability is needed to purposefully employ this degree of freedom. This is the basic motivation of our study. The floating zone configuration with little variation of the electrical conductivity simplifies the mathematical description of the flow driving magnetic force as compared to the case of a molten metal in an insulating container [6,7]. We obtain the magnetic force distribution in the low-frequency approximation that is relevant also for moderate dimensionless frequencies.

This range of frequencies is beneficial for the purpose of magnetic sonication since higher frequencies would cause more excess heating.

Induction heating together with a static magnetic field also has been considered in the floating zone growth of semiconductor crystals [8,9]. This configuration, however, is very much different from ours. The main differences include larger size and a more complicated shape of the domain, a high liquid-to-solid conductivity ratio, pronounced skin effect, and possible rotation. However, one feature is common, namely, the formation of the parallel $O(\mathrm{Ha}^{-1/2})$ layer (where Ha is the Hartmann number) [8] in a strong static field. This layer [10] is expected to govern the flow where it is strongest, that is, at the lateral edge of the domain. Thus, it should also govern the flow stability in the case of a strong static field. Our results confirm this picture and reveal the instability as a standing wave at the boundary between two flow tori within the parallel layer.

II. FORMULATION

A. Magnetic driving force

Consider a regular liquid metal cylinder of height $2z_0$ and radius r_0 bounded from top and bottom by semi-infinite solid nonmagnetic cylinders with the same radius and the same electrical conductivity σ [Fig. 1(a)]. Let this cylinder be immersed in a magnetic field with a constant axial component and an alternating component that varies slowly in the z direction [Fig. 1(b)]:

$$\boldsymbol{B}(r,z,t) = B_z\boldsymbol{e}_z + e^{i\omega t}\boldsymbol{\nabla}\times[\boldsymbol{e}_\phi A(r,z)], \tag{1}$$

where the complex vector potential amplitude $A(r,z) = A^\infty(r)[1-\epsilon(\frac{z}{z_0})^2]$ is expressed by the infinite cylinder solution [2]

$$A^\infty(r) = A_0 I_1\left(\sqrt{iS}\frac{r}{r_0}\right), \tag{2}$$

and $I_1(x)$ is the modified Bessel function of the first kind. The constant A_0 is determined by requiring $A(r_0) = B_0 r_0$:

$$A_0 = \frac{B_0 r_0}{\tilde{I}_1(\sqrt{iS})}, \tag{3}$$

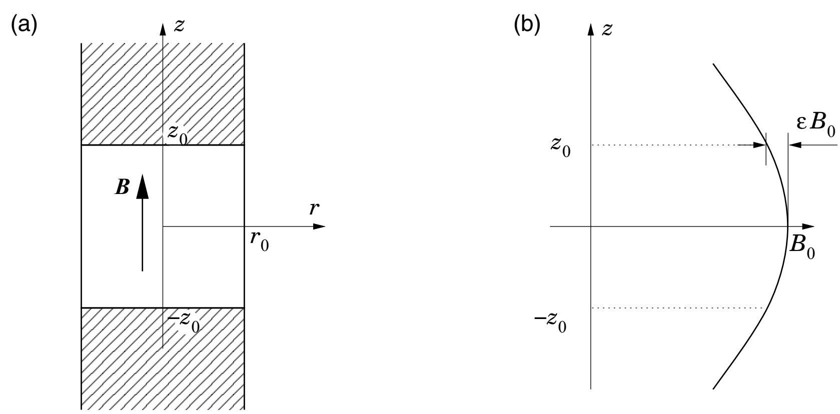

FIG. 1. (a) Scheme of the model; (b) variation of the alternating magnetic field induction along the cylinder surface.

where $\tilde{I}_1(x) = xI_1'(x) + I_1(x) = xI_0(x)$ and B_0 is the alternating magnetic field induction amplitude on the cylinder's surface at midheight $z = 0$. The dimensionless frequency or the shielding parameter

$$S = \mu_0 \sigma \omega r_0^2 \tag{4}$$

controls the penetration depth of the alternating magnetic field; μ_0 is the magnetic permeability of free space. Expression (1) is valid for $\epsilon \ll 1$ in cases when the induction coil is big and/or located far away from the cylinder as compared to the characteristic size z_0. The parameter

$$\epsilon = 1 - \frac{A(r_0,z_0)}{A(r_0,0)} \tag{5}$$

characterizes the deviation from a uniform distribution of the alternating magnetic field; see Fig. 1(b). The alternating magnetic field induces an alternating azimuthal electrical current with amplitude

$$j_\phi(r,z) = -i\sigma\omega A(r,z). \tag{6}$$

The cross product of it with the magnetic field produces the Lorentz force $\boldsymbol{F} = \boldsymbol{j} \times \boldsymbol{B}$. This force has an oscillating and a time-averaged part. It is assumed in this study that the oscillating magnetic force drives a rapidly oscillating flow that fully decouples from the mean flow. An estimate of the relevant condition is given in Sec. V. The time-averaged radial component of the magnetic force may be expressed as

$$F_r(r,z) = F_r^\infty(r)\left[1 - \epsilon\left(\frac{z}{z_0}\right)^2\right]^2, \tag{7}$$

where

$$F_r^\infty(r) = -0.5\sigma\omega\Re\left\{iA(r)\left[A'(r) + \frac{A(r)}{r}\right]^*\right\} = -0.5\sigma\omega B_0^2 r_0 \frac{\Re\left[iI_1\left(\sqrt{iS}\frac{r}{r_0}\right)\tilde{I}_1^*\left(\sqrt{iS}\frac{r}{r_0}\right)\right]}{|\tilde{I}_1(\sqrt{iS})|^2} \tag{8}$$

is the infinite cylinder solution for the mean radial magnetic body force and the asterisk superscript denotes complex conjugate. The melt flow is driven by the azimuthal curl of this force

$$(\nabla \times \boldsymbol{F}) \cdot \boldsymbol{e}_\phi = -4\epsilon F_r^\infty(r)\frac{z}{z_0^2}, \tag{9}$$

where quadratic ϵ terms are neglected. The value of the fraction expression on the right-hand side of (8) at $r = r_0$ is plotted in Fig. 2. In the low-frequency limit ($S \ll 1$) this expression may be approximated by $(S/16)(r/r_0)^3$ and (9) simplifies to

$$(\nabla \times F) \cdot \boldsymbol{e}_\phi \approx \epsilon\sigma\omega B_0^2 \frac{r_0}{z_0}\frac{S}{8}\left(\frac{r}{r_0}\right)^3 \frac{z}{z_0}. \tag{10}$$

In the high-frequency limit ($S \gg 1$) expression (9) simplifies to

$$(\nabla \times F) \cdot \boldsymbol{e}_\phi \approx \epsilon\sigma\omega B_0^2 \frac{r_0}{z_0}\sqrt{\frac{2}{S}}\exp[\sqrt{2S}(r/r_0 - 1)]\frac{z}{z_0}. \tag{11}$$

The characteristic value F_{curl} of both magnetic force curl expressions (10) and (11) may be combined and given in terms of the magnetic pressure $p_m = 0.5B_0^2/\mu_0$ as

$$F_{\text{curl}} = \frac{4\epsilon p_m}{z_0 r_0} S f_0(S), \tag{12}$$

where the function $f_0(S) \approx \min(S/16,(2S)^{-1/2})$ is displayed in Fig. 2.

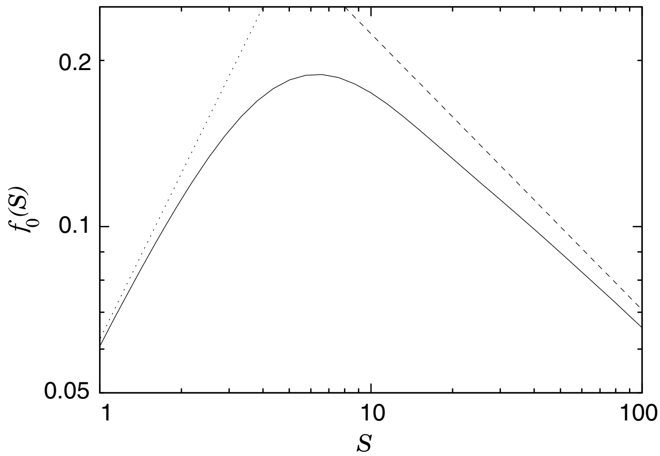

FIG. 2. Dependency of the alternating magnetic field induced force on the dimensionless frequency. Function $f_0(S)$ represents the value of the fraction expression on the right-hand side of (8) at $r = r_0$. The maximum of 0.18873 is reached at $S = 6.325$. Asymptotic solutions $S/16$ and $1/\sqrt{2S}$ are depicted by dotted and dashed lines, respectively.

B. Magnetic braking force

The alternating magnetic field-induced force (9) drives an axisymmetric meridional flow with velocity components $(U_r, 0, U_z)$. According to Ohm's law for a moving medium, such flow in an axial magnetic field produces an azimuthal electrical current

$$J_\phi = -\sigma U_r B_z, \tag{13}$$

which, in turn, produces a braking radial force

$$F_m(r,z) = (\boldsymbol{J} \times \boldsymbol{B}) \cdot \boldsymbol{e}_r = -\sigma U_r B_z^2. \tag{14}$$

The oscillating component of the magnetic field is neglected in the above expressions since it is much weaker than the constant one ($B_0 \ll B_z$) in the related application [2].

C. Basic flow

An axisymmetric meridional flow is conveniently described [11] by the modified stream function $H(r,z)$:

$$U_r(r,z) = -0.5r\frac{\partial H}{\partial z}, \quad U_z(r,z) = \left(H + 0.5r\frac{\partial H}{\partial r}\right). \tag{15}$$

By using z_0 or r_0 to scale the radial or axial distances and z_0^2/ν, ν/z_0 as the time and velocity scales, respectively (ν denotes the kinematic viscosity), the dimensionless stationary Navier-Stokes equation in terms of H and azimuthal vorticity W may be written as

$$\mathcal{N}(W) = \mathcal{L}(W) + \mathrm{Ha}^2\frac{\partial^2 H}{\partial z^2} + Fr^2 z, \tag{16}$$

$$\mathcal{L}(H) + 2W = 0, \tag{17}$$

where

$$\mathcal{L} = \frac{z_0^2}{r_0^2}\left(\frac{\partial^2}{\partial r^2} + \frac{3}{r}\frac{\partial}{\partial r}\right) + \frac{\partial^2}{\partial z^2}, \quad \mathcal{N} = U_r\frac{\partial}{\partial r} + U_z\frac{\partial}{\partial z}.$$

The no-slip boundary conditions for (16) and (17) are

$$H(z,\pm 1) = H(1,z) = \frac{\partial H}{\partial z}(z,\pm 1) = \frac{\partial H}{\partial r}(1,z) = 0. \tag{18}$$

Besides the aspect ratio r_0/z_0 there are two control parameters. The Hartmann number

$$\mathrm{Ha} = \sqrt{\frac{\sigma}{\rho\nu}}B_z z_0 \tag{19}$$

has the meaning of the dimensionless static field induction. The force parameter

$$F = \frac{F_{\mathrm{curl}} z_0^4}{\rho\nu^2} \tag{20}$$

expresses the dimensionless magnitude of the magnetic driving force curl (ρ is the density of the liquid). The radial dependency of the driving force in (16) assumes the low-frequency limit $S \ll 1$ (10) that is basically considered in this study. A few selected cases of moderate frequency $S \leqslant 20$ are also considered with the driving force radial dependency

$$\frac{1}{r}\frac{F_r^\infty(r)}{F_r^\infty(r_0)} \tag{21}$$

given by (8) instead of r^2 in (16). The value of the aspect ratio is fixed to $r_0/z_0 = 1$ in this study.

D. Flow perturbations

Suppose that we have found the solution $\boldsymbol{U}(r,z)$ of (16)–(18). To investigate its stability let us apply an infinitesimal three-dimensional perturbation $\boldsymbol{v}(r,\phi,z,t)$ and follow its development in time. The Navier-Stokes equation for such a perturbation may be written as

$$\frac{\partial \boldsymbol{v}}{\partial t} + \boldsymbol{\omega}\times\boldsymbol{U} + \boldsymbol{\Omega}\times\boldsymbol{v} = \nabla^2\boldsymbol{v} - \nabla P + \mathrm{Ha}^2(-\nabla\varphi + \boldsymbol{v}\times\boldsymbol{e}_z)\times\boldsymbol{e}_z, \tag{22}$$

$$\nabla\cdot\boldsymbol{v} = 0, \tag{23}$$

$$\nabla^2\varphi = \nabla\cdot(\boldsymbol{v}\times\boldsymbol{e}_z), \tag{24}$$

where $\varphi(r,\phi,z,t)$ is the electric potential perturbation and $\boldsymbol{\Omega} = \nabla\times\boldsymbol{U}$, $\boldsymbol{\omega} = \nabla\times\boldsymbol{v}$. On the surface of the liquid cylinder the no-slip boundary conditions are applied for the velocity perturbation $\boldsymbol{v} = 0$, and the radial derivative of the electrical potential is set to zero,

$$\left.\frac{\partial\varphi}{\partial r}\right|_{r=1} = 0, \tag{25}$$

on the surface of the whole conducting cylinder. The three-dimensional electrical currents created by the flow perturbation in the static field are not bound to the domain of the liquid metal, and they may leak into the solid semi-infinite cylinders. Thus, the potential equation (24) should be also solved there,

$$\nabla^2\varphi = 0, \tag{26}$$

together with continuity of φ and $\partial\varphi/\partial z$ at $z = \pm 1$. These continuity conditions may be expressed as Robin's boundary conditions for separate axial modes used for the solution in the liquid domain by the diagonalization technique. These conditions are given in Sec. III C. They allow us to account for the solution of (26) in the solid cylinders without actually solving it.

III. SOLUTION TECHNIQUES

A. Basic flow

We used slightly modified spectral numerical simulation codes developed and tested for a similar problem [11]. The solution was sought in the form of Chebyshev polynomial series. The basic flow was calculated by time integration of (16) and (17). A second order implicit backward differentiation formula [12] was used. The problem, thus, was reduced to a repeated solution of the Helmholtz-type equation in the form

$$\mathcal{L}(W^{n+1}) - \frac{3}{2\Delta t}W^{n+1} = W_s \tag{27}$$

for W^{n+1} and the Poisson-type equation (17) for H^{n+1} in the new time layer. These equations were solved by the diagonalization technique [13] in the radial direction and fast factorization in the axial direction. There are two boundary conditions for H (18) and none for W. This disparity was resolved by the so-called capacitance matrix, which establishes a relation between the Dirichlet boundary conditions for W and the respective Neumann conditions for H. The vorticity $\tilde{W}$ was first found as a solution of (27) with zero Dirichlet conditions. The respective stream function $\tilde{H}$ was then calculated from (17) with only the Dirichlet conditions applied. The residual in the Neumann conditions for $\tilde{H}$ was then translated into boundary conditions for the vorticity correction W_c by the inverse of the capacitance matrix. The respective corrected stream function $\tilde{H} + H_c$ then satisfied both boundary conditions (18).

B. Perturbations

Given the basic flow the perturbation equations (22)–(24) were integrated in time for separate normal azimuthal modes $\boldsymbol{v}^m(r,z,t)$,

$$\boldsymbol{v}(r,\phi,z,t) = \Re\left[\sum_{m=1}^{M} \boldsymbol{v}^m(r,z,t)\exp(im\phi)\right], \tag{28}$$

following Ref. [11]. By a third order implicit backward differentiation formula [12] these equations transform into repeated Helmholtz equations for the velocity perturbation field and a Poisson equation (with unknown boundary conditions) for the pressure perturbation. The pressure boundary conditions were evaluated by resolving the capacitance matrix linking them to the residual of the velocity field divergence at the edge of the liquid domain. The perturbation equations (22)–(24) were integrated in time from a random divergence free initial condition to produce a set of $N = 15$ "snapshots" that were decomposed into leading eigenmodes

$$\boldsymbol{v}^m(r,z,t) \approx \sum_{n=1}^{N-1} \boldsymbol{v}_n^m(r,z)\exp(\lambda_n t) \tag{29}$$

following Ref. [14]. The obtained eigenvalue with the maximum real part was compared to the one obtained from the preceding set of 15 "snapshots." The calculations were stopped when the scaled difference was less than 10^{-5}. The separation of the "snapshots" was 100 to 200 time steps and typically measured a few percent of the oscillation period. The spatial resolution was 73 axial and 43 radial modes for $\mathrm{Ha} < 300$. It was increased to 97×65 for $300 \leqslant \mathrm{Ha} < 700$ and 129×83 modes for $\mathrm{Ha} \geqslant 700$. The time step was between 4×10^{-6} for $\mathrm{Ha} = 10$ and 0.1×10^{-6} for $\mathrm{Ha} = 1000$.

The above described algorithm produced the leading eigenvalue $\lambda = \lambda_r + i\lambda_i$ as a function of the azimuthal wave number m and control parameters F, Ha. The flow is linearly stable if λ_r is negative for all m. The critical force $F_{cr}(\mathrm{Ha})$ was evaluated as the minimum root of $\lambda_r(F,\mathrm{Ha},m)$ from $m \in [1 : M]$. The upper bound M of this range was gradually increased with Ha from $M = 9$ at $\mathrm{Ha} = 10$ to $M = 60$ at $\mathrm{Ha} = 1000$. The obtained instability results were cross-checked by the full three-dimensional spectral solution [15] for a few combinations of the control parameters.

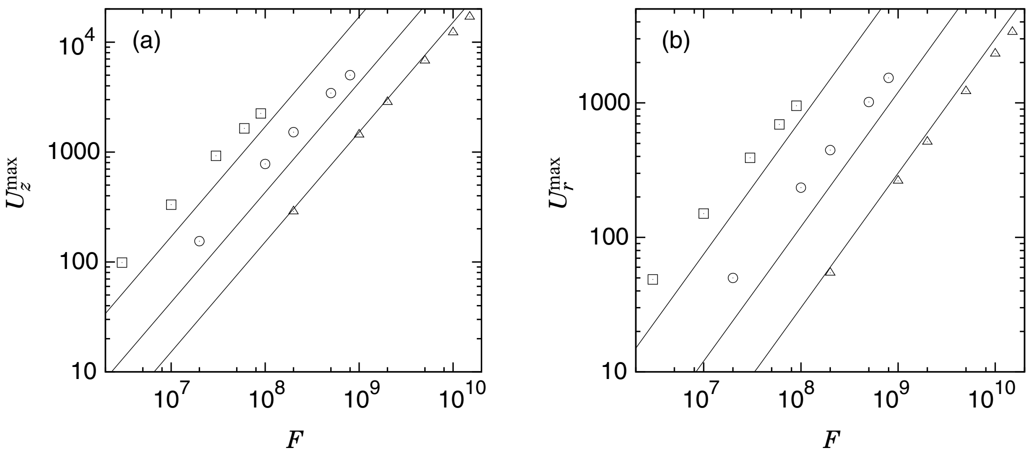

FIG. 3. Maximum (a) axial and (b) radial velocity vs the driving force at different static field strengths. Boxes, circles, and triangles correspond to Ha = 200, 500, and 1000, respectively. Solid lines display the functions $0.048F\,\mathrm{Ha}^{-3/2}$ and $0.3F\,\mathrm{Ha}^{-2}$ in (a) and (b), respectively.

C. Potential boundary conditions

The diagonalization technique is the discrete analog of the variable separation method by which the solution of (24) or (26) is sought as

$$\varphi(r,z) = \sum_j Z_j(z)R_j(r), \tag{30}$$

where $R_j(r)$ are eigenfunctions of the radial part of the Laplace operator satisfying

$$R_j'' + \frac{R_j'}{r} - \frac{m^2 R_j}{r^2} = \gamma_j R_j, \quad R_j'(1) = 0 \tag{31}$$

and $\gamma_j \leqslant 0$ are the respective eigenvalues. The axial functions $Z_j(z)$ for the solution of (26) satisfy

$$Z_j'' + \gamma_j Z_j = 0 \tag{32}$$

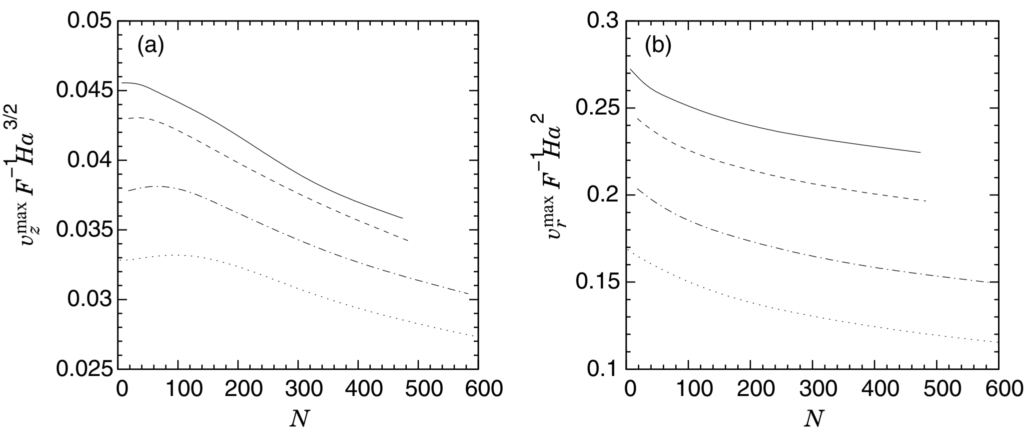

FIG. 4. Maximum (a) axial and (b) radial velocity vs the interaction parameter $N = F\,\mathrm{Ha}^{-5/2}$ at different Ha. Solid, dashed, dash-dotted, and dotted lines correspond to Ha = 1000, 500, 200, and 100, respectively.

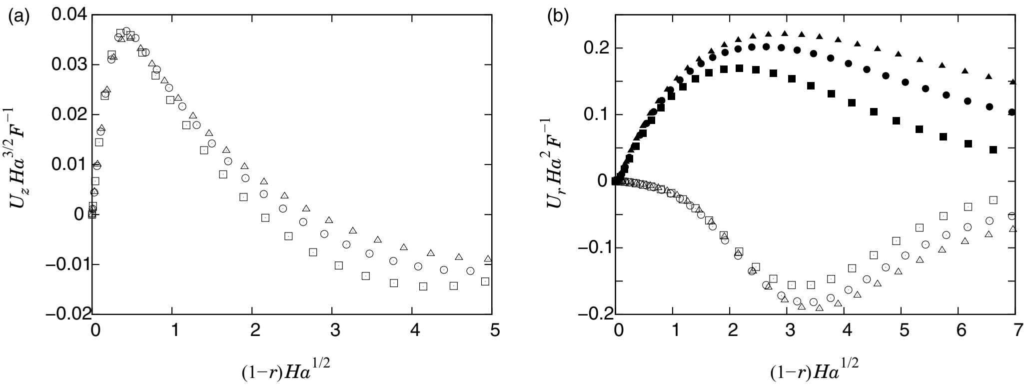

FIG. 5. Scaled radial profiles of (a) axial velocity at $z = -0.5$; (b) radial velocity at $z = 0$ (open symbols) or near the end wall ($z \approx 1$, filled symbols). Boxes, circles, and triangles correspond to (Ha $= 200$, $F = 10^8$), (Ha $= 500$, $F = 10^9$), and (Ha $= 1000$, $F = 5 \times 10^9$), respectively.

with the general solution $Z_j(z) = c_j \exp(-\sqrt{-\gamma_j} z)$ in the upper solid cylinder. The axial derivative there satisfies $Z_j'(z) = -\sqrt{-\gamma_j} Z_j(z)$. Consequently, the continuity conditions at $z = \pm 1$ for the solution of (24) in the form (30) may be given as

$$\sqrt{-\gamma_j} Z_j(\pm 1) \pm Z_j'(\pm 1) = 0, \tag{33}$$

thus fully decoupling the liquid domain.

IV. RESULTS

A magnetic field strength of up to Ha $= 1000$ is considered in this study. This corresponds to about 2.5 T for aluminum and 8 T for steel in a 1 cm radius sample.

A. Basic flow

The ac-induced mean body force (7) drives two symmetrical counter-rotating tori with inward-directed radial velocity at the midplane. A nearly linear scaling with the driving force magnitude F was observed for the maximum values of the axial and radial velocities in a strong static field $\mathrm{Ha}^{1/2} \gg 1$ (Fig. 3). Figure 4 displays essentially the same information in a manner that better reveals the deviation from the linear behavior. A considerable deviation from the linear scaling was observed

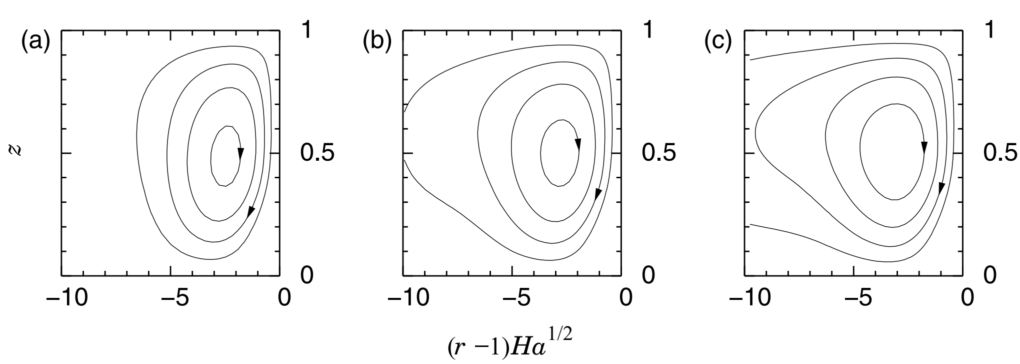

FIG. 6. Streamlines of the basic flow in near-critical state for (a) Ha $= 200$, $F = 3.3 \times 10^8$; (b) Ha $= 500$, $F = 2.66 \times 10^9$; (c) Ha $= 1000$, $F = 1.48 \times 10^{10}$. The streamline spacing is scaled by $\mathrm{Ha}^{1/2}$.

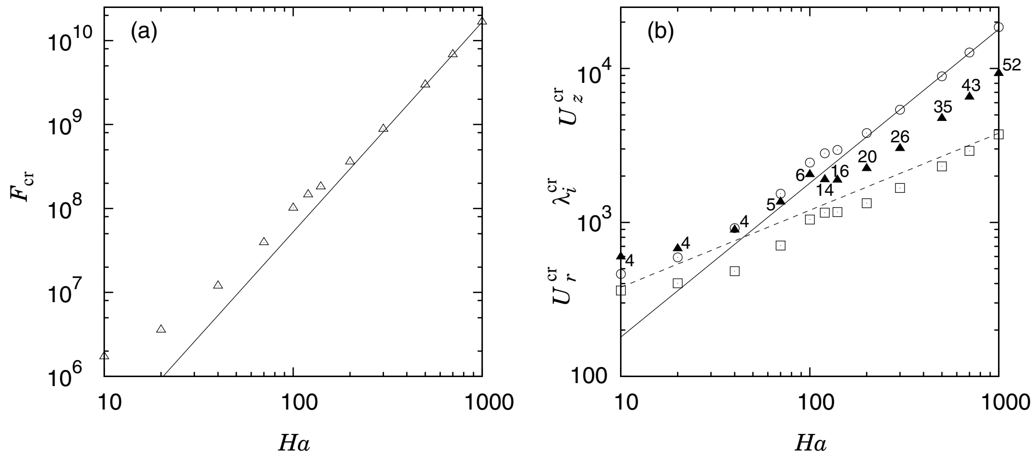

FIG. 7. Dependency of the critical parameters on the static magnetic field strength: (a) The critical force; (b) oscillation frequency (triangles) and the maximum axial (circles) or radial (boxes) critical flow velocity. The line in (a) displays the function $525\mathrm{Ha}^{5/2}$. Functions 18Ha and $120\mathrm{Ha}^{1/2}$ are depicted by solid and dashed lines in (b). Numbers in (b) display the azimuthal wave number m of the critical perturbation.

as the interaction parameter defined as $N = F\,\mathrm{Ha}^{-5/2}$ reached a value of several hundreds. We shall see in Sec. IV B that this is accompanied by the instability onset at $N \approx 525$. The dependency of the maximum axial and radial velocity on the magnetic field strength followed $O(\mathrm{Ha}^{-3/2})$ and $O(\mathrm{Ha}^{-2})$ scalings. This is consistent with the formation of $O(\mathrm{Ha}^{-1/2})$ side layers illustrated by Fig. 5. The flow distribution in these layers is displayed in Fig. 6.

B. Instability

The critical force parameter dependency $F_{cr}(\mathrm{Ha})$ is shown in Fig. 7(a). A transition from the bulk instability mode characterized by comparably low wave number $m \leqslant 6$ [Fig. 8(a)] to the side layer instability mode with a high $m \geqslant 14$ and $F_{cr} \approx 525\mathrm{Ha}^{2/5}$ was observed near Ha = 110 [Fig. 8(b)].

The high Ha side layer instability mode is further explored in Figs. 9 and 10. It was always oscillatory with two complex conjugated leading eigenvalues. Its symmetry with respect to the

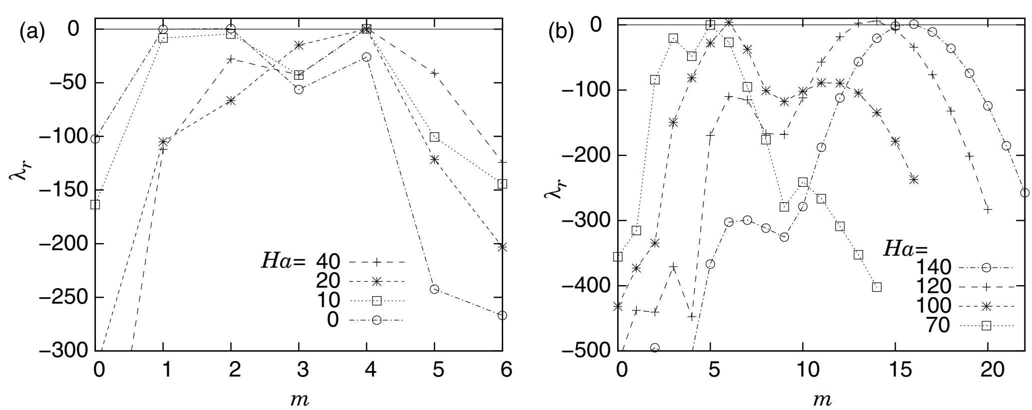

FIG. 8. Dependency of the real part of the leading eigenmode on the perturbation azimuthal wave number m near the instability onset for (a) low Ha $\leqslant 40$ and (b) intermediate to high Ha $\geqslant 70$.

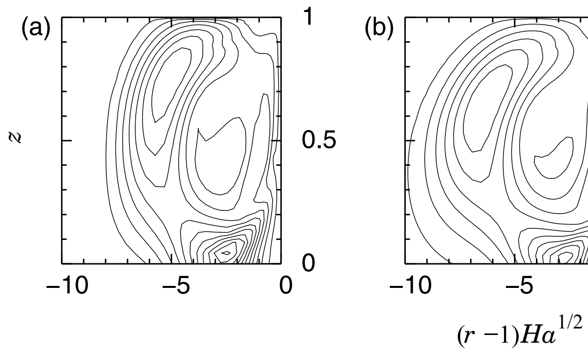

FIG. 9. Boundary layer mode: Isolines of the velocity amplitude for the critical perturbation at (a) Ha $= 200$, $F = 3.61 \times 10^8$, $m = 20$; (b) Ha $= 500$, $F = 3.0 \times 10^9$, $m = 35$; (c) Ha $= 1000$, $F = 1.67 \times 10^{10}$, $m = 52$.

midplane was opposite to that of the basic flow. The azimuthal wave number m increased as $\propto \mathrm{Ha}^{1/2}$ to a staggering value of $m = 52$ at Ha $= 1000$. That may be translated into approximately constant wave length expressed in units of the parallel layer thickness as $2\pi/m \approx 3.82\mathrm{Ha}^{-1/2}$. The velocity maximum was located on the midplane at a distance about $3\mathrm{Ha}^{-1/2}$ from the lateral boundary (Fig. 9). This maximum coincided approximately with the basic flow maximum for the radial velocity (Fig. 5). The axial velocity component increasingly dominated as the side boundary layer became thinner for increasing Ha [cf. Figs. 9(c) and 10(c)]. The oscillation frequency λ_i^{cr} correlated with the maximum axial velocity U_z^{cr} staying approximately half of the latter.

The bulk instability mode is shown in Fig. 11. It was similar to the boundary layer mode in that it also had a maximum of the critical perturbation axial velocity at the midplane. This mode was oscillatory too. The frequency was approximately equal to the maximum axial velocity of the base flow [Fig. 7(b)]. The wave number m, in turn, was about a half of what would be the wave number of the corresponding boundary layer mode. Competition between both modes manifested itself as a "double-humped" $\lambda_r(m)$ dependency in the intermediate Ha range [Fig. 8(b)].

For Ha $= 0$ the instability character changed radically. The first instability was monotonic ($\lambda_i = 0$) at $F_{cr} = 0.927 \times 10^6$ with very close $m = 2$ and $m = 1$ modes [Fig. 8(a)]. The most unstable $m = 2$ mode had the vertical symmetry of the basic flow, while the follow-up $m = 1$ mode was symmetry-breaking. They both retained a high growth rate also for Ha $= 10$.

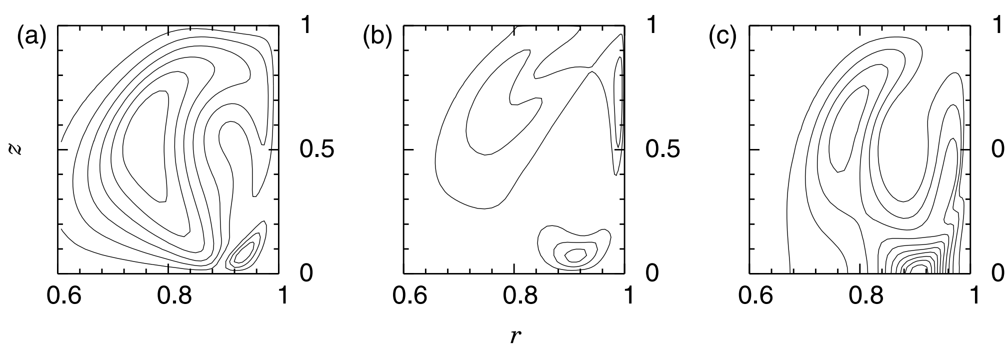

FIG. 10. Isolines of amplitude of the critical velocity perturbation components for Ha $= 1000$, $F = 1.67 \times 10^{10}$, $m = 52$. Radial, azimuthal, and axial velocity perturbation displayed in panels (a)–(c), respectively. Isoline spacing in panel (c) is five times larger than in panels (a) and (b).

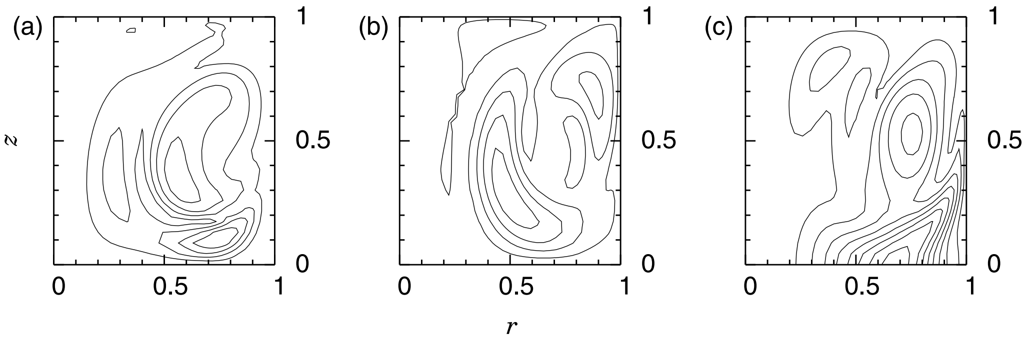

FIG. 11. Bulk mode: Isolines of amplitude the critical velocity perturbation components for Ha $= 40$, $F = 1.2 \times 10^7, m = 4$. The radial, azimuthal and axial velocity amplitude is displayed in panels (a)–(c), respectively, with an equal isoline spacing.

V. DISCUSSION

The flow under consideration forms as a side effect of the magnetic sonication within a liquid metal zone by strong alternating and static axial magnetic fields. The finite length of the induction coil causes some axial variation of the alternating magnetic field amplitude characterized by a small parameter ϵ. We expand it in a Taylor series and retain only the quadratic term as the linear term is assumed zero because of the symmetry of the magnetic and heat removal systems. This approach allows us to decouple details of any particular induction coil configuration and "condense" them into a single parameter. The effect of a different electrical conductivity in the solid parts of the sample may also be taken into account by this approach if the skin effect is moderate.

Accuracy of the model may be gauged by deviation from the assumed parabolic profile of the ac field. To apply the results of the current study for any particular configuration ϵ needs to be estimated somehow. For this purpose the induction heating problem may be solved separately. This was done by the numerical simulation software COMSOL for the configuration of the experiment in Ref. [2] with a stainless steel sample. The scaled variation of the alternating magnetic field induction along the surface of the liquid zone was found as $\epsilon \approx 0.1$.

Since the alternating magnetic field is stronger at the midplane, the molten metal is pushed inwards there creating two symmetrical tori. Under a strong magnetic field those tori develop pronounced parallel layers (Fig. 5), while their intensity scales almost linearly with the flow-driving radial force measured by F (Fig. 3). The maximum radial flow velocity scales $\propto \mathrm{Ha}^{-2}$ while the axial velocity is by a factor $O(\mathrm{Ha}^{1/2})$ larger. The difference is caused by the flow continuity condition as the radial flow varies in the radial direction within a characteristic distance of $O(\mathrm{Ha}^{-1/2})$, while the vertical distance of the corresponding axial velocity variation is not influenced by Ha.

There are three linear instability onset modes. Two of them (Ha $\geqslant 10$) are symmetry-breaking and oscillatory. They appear related as the boundary layer mode (Fig. 10) is similar in shape to the bulk mode (Fig. 11) just being squeezed to the parallel layer. These modes differ by the wave length expressed in units of the parallel layer thickness. It is described by the quantity $2\pi \mathrm{Ha}^{1/2}/m$, which drops by a factor of about 0.5 as the bulk mode is replaced by the boundary layer mode at Ha ≈ 110. Simultaneously, the oscillation frequency expressed in units of the maximum base flow velocity (quantity λ_i^{cr}/U_z^{cr}) drops also by a factor ≈ 0.5. The third instability mode for small Ha < 10 is symmetrical and monotonic.

Practically the most important regime is that of a high Ha $\geqslant 120$ characterized by a high azimuthal wave number of the instability. The energy of the critical perturbation is basically concentrated in the axial velocity component on the midplane at a distance about $3\mathrm{Ha}^{-1/2}$ from the side boundary (Figs. 9 and 10). This coincides with the maximum of the radial velocity of the basic flow [Fig. 5(b)]. Another maximum of the critical perturbation is apparently formed by the returning axial flow at

TABLE I. Comparison of the critical parameters with the low-frequency $S \ll 1$ force expression (10) and the general expression (9) at $S = 20$.

	F_{cr}		λ_i^{cr}		m	
Ha	$S \ll 1$	$S = 20$	$S \ll 1$	$S = 20$	$S \ll 1$	$S = 20$
40	1.19×10^7	1.45×10^7	895.5	0	4	2
200	3.61×10^8	4.38×10^8	2242	2190	20	21
1000	1.68×10^{10}	1.75×10^{10}	9294	8856	52	54

$|z| \approx 0.5$ at a distance about $7\text{Ha}^{-1/2}$ from the side boundary [Figs. 9(b) and 9(c)]. This instability may be imagined as a standing azimuthal wave on the boundary separating the two basic flow tori. As the critical flow conditions are passed several modes with close azimuthal wave number m may become unstable [Fig. 8(b)]. This is expected to excite a growing wave packet instead of a uniform wave.

The high-Ha instability sets in when the interaction parameter $N = F\,\text{Ha}^{-5/2}$ reaches a value of about 525 [Fig. 7(a)]. Scaling of F_{cr} in Fig. 7(a) and the similarity in Figs. 5 and 9 suggests that this instability mode might be well described by an asymptotic parallel layer solution for $\text{Ha} \geqslant 120$. If so, then the effect of the aspect ratio should be limited to its influence on the flow-driving curl (10). This expression is proportional to r_0/z_0. Thus, the critical dimensionless force (20) should be inversely proportional to r_0/z_0 while the azimuthal wave number should increase linearly with the aspect ratio. We tested this conjecture with an example at $\text{Ha} = 200$, $r_0/z_0 = 2$ and found $F_{cr} = 1.53 \times 10^8$, $\lambda_i^{cr} = 1946$, and $m = 46$. This agrees with the values $F_{cr}/2 = 1.8 \times 10^8$, $\lambda_i^{cr} = 2242$, and $2m = 40$ at $\text{Ha} = 200$, $r_0/z_0 = 1$ within 15% (Table I).

Let us consider as an example the configuration in Ref. [2] with $\epsilon \approx 0.1$, $r_0 = 10^{-2}$ m, $\omega = 0.9 \times 10^5\ \text{s}^{-1}$, $B_0 = 0.13$ T, $B_z = 0.5$ T, and a stainless steel sample ($\nu = 0.8 \times 10^{-6}\ \text{m}^2/\text{s}$, $\rho = 7 \times 10^3\ \text{kg/m}^3$, $\sigma = 0.72 \times 10^6$ S/m [16]). The dimensionless frequency (4) is $S = 8$, and the characteristic magnetic curl (12) $F_{\text{curl}} = 4 \times 10^7\ \text{N/m}^4$ ($f_0(8) = 0.185$). The Hartmann number (19) is $\text{Ha} = 57$ and the force parameter (20) $F = 1.2 \times 10^8$. From Fig. 7 it may be estimated that the regime should be unstable with $F \approx 5F_{cr}(\text{Ha})$. The flow stabilization may be possible at $\text{Ha} \approx 110$ or $B_z \approx 1$ T with the maximum velocity as high as 0.2 m/s.

The driving force expression (10) assumes $S \ll 1$. As the dimensionless frequency S increases, the radial dependency of the driving force gradually transforms towards (11). Simultaneously, the low-frequency results should become less relevant. To get an idea how far they can still be applied we replaced (10) with (9) at $S = 20$ for $\text{Ha} = 40$, 200, and 1000. The comparisons to the low-frequency results are given in Table I. For the selected parameter values the difference in F_{cr} remained below 20% and was as small as 5% at $\text{Ha} = 1000$. A smaller difference at a higher Ha is explained by a smaller variation of the driving force within the parallel layer. In the low-Ha range, in turn, the skin effect may even change the onset mode to the monotonic one as was observed at $\text{Ha} = 40$.

One of the core assumptions of the model concerns negligible effect of the oscillating flow $\boldsymbol{v}'$. This is valid as long as the dynamical pressure of the oscillating flow remains much lower than the time-averaged flow-driving magnetic pressure:

$$\rho v'^2 \ll \epsilon \frac{B_0^2}{\mu_0}. \tag{34}$$

The magnitude of the oscillating flow v' may be estimated comparing inertia to the oscillating magnetic pressure [2]:

$$\rho \omega z_0 v' = O\left(\epsilon \frac{B_0 B_z}{\mu_0}\right). \tag{35}$$

Combining these expressions produces

$$\epsilon \frac{B_z^2}{\mu_0} \ll \rho\omega^2 z_0^2, \tag{36}$$

which is easily satisfied in the experiment [2] for any practically feasible B_z. However, the quadratic dependency on ac frequency and sample size suggests that up-scaling may change this. Besides, it may not be excluded that even a relatively small time-averaged contribution of the oscillating flow disproportionally influences the instability onset. The question of the oscillating flow effect emerges as the central one for a practically oriented continuation of the current study.

VI. SUMMARY

The floating zone configuration with a small variation of the electrical conductivity upon melting allows for a simple model of the flow driving force. This force produces two symmetrical flow tori. The superimposed strong static axial magnetic field creates a pronounced parallel layer for $\mathrm{Ha} \geqslant 120$. In this regime the flow instability sets in as a symmetry-breaking standing wave with a high azimuthal wave number when the interaction parameter $N = F\,\mathrm{Ha}^{-5/2}$ reaches a value of about 525. The low-frequency model of the driving force (10) remains relevant for the dimensionless frequency (4) up to $S \approx 20$.

ACKNOWLEDGMENTS

D. Berenis has calculated the value of $\epsilon \approx 0.1$ by the multiphysics simulation software COMSOL for the configuration of experiment [2] with a stainless steel sample. Financial support from German Helmholtz Association in framework of the Helmholtz Alliance Liquid Metal Technologies (LIMTECH) Project (No. HA-315) is gratefully acknowledged. I.G. was also supported by University of Latvia under Grant “Combined electromagnetic field impact during semi-continuous crystallization for high performance alloy production” (No. 6012-A55.2/48).

---

[1] Q. Wang, T. Momiyama, K. Iwai, and S. Asai, Non-contact generation of intense compression waves in a molten metal by using a high magnetic field, Mater. Trans., JIM **41**, 1034 (2000).

[2] I. Grants, A. Bojarevičs, and G. Gerbeth, Contactless magnetic excitation of acoustic cavitation in liquid metals, J. Appl. Phys. **117**, 204901 (2015).

[3] I. Kaldre, A. Bojarevičs, I. Grants, T. Beinerts, M. Kalvans, M. Milgravis, and G. Gerbeth, Nanoparticle dispersion in liquid metals by electromagnetically induced acoustic cavitation, Acta Mater. **118**, 253 (2016).

[4] X. Li, Y. Yang, and D. Weiss, Theoretical and experimental study on ultrasonic dispersion of nanoparticles for strengthening cast aluminum alloy A356, Metallurgical Sci. Technol. **26**, 12 (2008).

[5] S. Jia, D. Zhang, and L. Nastac, Experimental and numerical analysis of the 6061-based nanocomposites fabricated via ultrasonic processing, J. Mater. Eng. Perform. **24**, 2225 (2015).

[6] V. Shatrov, G. Gerbeth, and R. Hermann, Linear stability of an alternating-magnetic-field-driven flow in a spinning cylindrical container, Phys. Rev. E **77**, 046307 (2008).

[7] A. Cramer, V. Galindo, and M. Zennaro, Frequency dependence of an alternating magnetic field driven flow, Magnetohydrodynamics **51**, 133 (2015).

[8] K. H. Lie, J. S. Walker, and D. N. Riahi, Melt motion in the float zone process with an axial magnetic field, J. Cryst. Growth **109**, 167 (1991).

[9] G. Raming, A. Muižnieks, and A. Mühlbauer, Numerical investigation of the influence of EM-fields on fluid motion and resistivity distribution during floating-zone growth of large silicon single crystals, J. Cryst. Growth **230**, 108 (2001).

[10] U. Müller and L. Bühler, *Magnetofluiddynamics in Channels and Containers* (Springer, Berlin, 2001).

[11] I. Grants and G. Gerbeth, Stability of melt flow due to a traveling magnetic field in a closed ampoule, J. Cryst. Growth **269**, 630 (2004).

[12] J. P. Boyd, *Chebyshev and Fourier Spectral Methods*, 2nd ed. (Dover Publications, New York, 2000).

[13] C. Canuto, M. Y. Hussaini, A. Quarteroni, and T. A. Zhang, *Spectral Methods in Fluid Dynamics* (Springer, New York, 1988).

[14] I. Goldhirsch, S. A. Orszag, and B. K. Maulik, An efficient method for computing leading eigenvalues and eigenvectors of large asymmetric matrices, J. Sci. Computing **2**, 33 (1987).

[15] I. Grants and G. Gerbeth, Linear and nonlinear stability of a thermally stratified magnetically driven rotating flow in a cylinder, Phys. Rev. E **82**, 016314 (2010).

[16] E. A. Brandes and G. B. Brook (eds.), *Smithells Metals Reference Book*, 7th ed. (Butterworth-Heinemann, Oxford, 1992).